Comparison of rainfall estimates from GPM dual-frequency precipitation radar and ground dual-polarization radar

L. L. Kou[1,2,3], Y. Mao[3], Z. X. Wang[3], Y. Chen[3], Z. G. Chu[2,3], and A. J. Chen[1,2,3]

[1] Collaborative Innovation Center on Forecast and Evaluation of Meteorological Disasters, Nanjing University of Information Science and Technology, Nanjing, China

[2] Key Laboratory for Aerosol-Cloud-Precipitation of China Meteorological Administration, Nanjing University of Information Science and Technology, Nanjing, China

[3] School of Atmospheric Physics, Nanjing University of Information Science and Technology, Nanjing, China

Corresponding author: Leilei Kou (cassie320@163.com)

Key Points:

- Matched scan mode: best rainfall estimation performance for liquid samples and better mass-weighted mean diameter estimation
- High sensitivity scan mode: good consistency for stratiform precipitation estimation, but poor for convective precipitation estimation
- Rainfall estimation based on hydrometeor phases meaningful for both DPR and ground dual-polarization radar

Abstract

The dual-frequency precipitation radar (DPR) onboard the Global Precipitation Measurement (GPM) core satellite can provide information on drop size distribution (DSD) to improve rainfall estimation. The ground-based dual-polarization radar has great advantages for rainfall estimation, owing to the greater accessibility to information about the DSD and hydrometeor type. In this study, the three-dimensional rainfall products from DPR, with normal scan (NS), matched scan (MS), and high sensitivity scan (HS) mode, and C-band dual-polarization radar (CDP) were compared based on the volume matching algorithm and hydrometeor identification. The reliability of CDP rainfall and DSD parameter estimation for liquid samples was evaluated using rain gauge and disdrometer data. Rainfall relations for non-liquid samples for CDP were obtained via scattering simulation. An intercomparison of reflectivity revealed correlations of more than 0.8 for all three DPR scanning modes for stratiform and convective precipitation. Rainfall comparison performance of the MS mode was slightly better than that of the NS mode for liquid samples, especially for convective precipitation, which may be attributed to MS mode having the best consistency of mass-weighted mean diameter estimation. The HS mode showed good agreement, with respect to stratiform rainfall, but poor agreement, with respect to convective rainfall. For non-liquid samples, the biases were within 0.8 mm/h. The NS mode showed the best agreement, followed by the HS mode; however, the consistency was worse than that for liquid samples. Given the different physical characteristics of hydrometeors, our findings highlight the importance of rainfall estimation based on hydrometeor phases.

1 Introduction

Accurate rainfall estimation is essential in various applications, including flood estimation, water resource management, weather forecasting, agriculture, and understanding the cycling of global water (Camille et al., 2020; Cannon et al., 2017). Precipitation radar (PR) carried on the satellite view from top to bottom, which can provide quasi-global three-dimensional (3D) precipitation measurement (Kou et al., 2018; Skofronick-Jackson et al., 2017; Tang et al., 2017). The PR onboard the Tropical Rainfall Measuring Mission (TRMM) satellite was the first spaceborne weather radar. It has provided a large amount of precipitation data, enabling scientific studies and societal benefits over the tropics. With the success of TRMM, the Global Precipitation Measurement Mission (GPM) core satellite was launched in February 2014. The dual-frequency

precipitation radar (DPR) on the GPM operates at 13.6 GHz (Ku-band) and 35.5 GHz (Ka-band). Through dual-band measurement, the DPR can obtain the drop size distribution (DSD) information and improve the accuracy of quantitative precipitation estimation (Hou et al., 2014; Skofronick-Jackson et al., 2018). In addition, compared with TRMM, the coverage of DPR was extended to $\pm 65°$, and the ability to detect weak and strong precipitation was further strengthened.

To evaluate and verify the performance of precipitation products measured by spaceborne radar for better applications, it is essential to compare and validate the precipitation data of spaceborne radar based on ground-measured data. After the launch of the GPM, GPM ground validation field campaigns were carried out, e.g., the Integrated Precipitation and Hydrology Experiment (IPHEx) and the Olympic Mountains Experiment (OLYMPEx) (Barros et al., 2014; Houze et al., 2017). OLYMPEx evaluated the GPM satellite rainfall retrieval algorithm and hydrological application of precipitation products in the Washington area, based on S-band dual-polarization radar, rain gauge, and other ground observations (Houze et al., 2017). Studies conducted globally have performed validation tests and data comparison (D'Adderio et al., 2018; Gao et al., 2021; Jiang et al., 2020; Liao & Meneghini, 2019; Pettacra et al, 2018; Watters et al., 2018; Zhang et al., 2019). Lasser et al. (2019) evaluated three types of DPR surface rainfall products based on a local-scale terrestrial network of 153 meteorological stations in southeastern Austria. The results showed that the DPR has good consistency with ground stations. Ka-MS was noted to perform the best because of the higher number of light rain events. Speirs et al. (2017) evaluated the estimated surface precipitation products of the DPR in complex terrain over Switzerland against measurements from a C-band operational radar network. D'Adderio et al. (2019) compared the single-frequency (SF) and double-frequency (DF) PR products over the Mediterranean area to investigate the reliability of SF-based products with DF-based products as references. Biswas et al. (2018) cross-validated reflectivity measurements at the Ku- and Ka-bands and DPR instantaneous rain rate products against five dual-polarization radars from the GPM GV network, which showed that the matched DPR and GR reflectivity were in good agreement. Liao et al. (2014) assessed the uncertainties of DSD parameters employed in DPR precipitation retrievals. The study pointed out that DPR provides accurate rainfall and attenuation estimates with a fixed-μ gamma DSD model.

Ground-based dual-polarization radar is advantageous for quantitative precipitation estimation because of its potential to characterize precipitation microphysics and identify different hydrometeor types (Bringi et al., 2001; Chandrasekar et al., 2008; Liu et al., 2007). The optimal DSD parameters and hydrometeor classification can be obtained using a certain retrieval algorithm using polarization information (Cao et al., 2010; Huang et al., 2020; Mahale et al., 2019; Zhang et al., 2001). In addition, a dual-polarization radar system can provide measurements that are immune to absolute radar calibration and partial beam blockage and can further improve the accuracy of rainfall estimation (Bringi et al., 2001; Chen et al., 2017). With these advantages, dual-polarization radar is a powerful tool that can cross-validate the precipitation products and the microphysical properties parameterized in DPR. In our studies, the 3D rainfall products of DPR with different scanning modes, precipitation types, and precipitation phases were compared with the rainfall estimation from C-band ground-based dual-polarization radar (CDP). The reflectivity factors (hereafter called reflectivity) and retrieval DSD parameters from the dual-polarization radar are also used to assess parameters in the evolving DPR precipitation retrieval algorithm. The reliabilities of ground-based dual-polarization radar estimations for liquid samples have been tested using rain gauge and disdrometer data. The main goal of such comparative studies is to analyze the differences between different precipitation products of DPR under various precipitation conditions and provide a possible indication for the improvement of DPR precipitation retrieval. On the other hand, comparative research helps to understand the characteristics of different observation data better and utilize the various advantages of different sensors to yield an optimal multisensor estimate of rainfall.

This paper is organized as follows: Section II provides an overview of the data set considered, in addition to brief descriptions of hydrometeor classification, rainfall estimation, and mass-weighted mean diameter (D_m) retrieval of CDP. The optimal rainfall estimation of CDP was validated using rain gauge data. The D_m retrieval of CDP was also tested using the disdrometer data. In Section III, the comparison results are presented. First, the comparisons of bright band (BB) height and phase identification from DPR and CDP are shown. Second, the measurement data of reflectivity from CDP and DPR are compared based on the volume matching method, and the band conversion is considered. Then, quantitative comparisons of rainfall estimates are reported for DPR in NS, MS, and HS modes for different precipitation types and precipitation phases concerning the optimal rainfall estimation of CDP. Finally, Section V concludes the paper.

2 Datasets and Methods

2.1 DPR products

The GPM DPR consists of two radars operating in the Ku-band (35.5 GHz) and Ka-band (13.6 GHz). One reason for adding the Ka-band is to obtain DSD retrievals based on different scattering and attenuation effects at the Ka- and Ku-bands (Hou et al., 2014; Seto et al., 2013). A major source of error in rainfall estimates from TRMM PR is the uncertainty in the conversion of radar reflectivity into rainfall rate, mainly caused by variations in the DSDs that change by region and rain type (Liao et al., 2014). More detailed microphysical information from the DPR could lead to improved rainfall estimates. The dual-band returns will also allow us to distinguish regions of liquid, frozen, and mixed-phase precipitation (Le et al., 2013). Another reason for adding the Ka-band is to improve the detection thresholds for light rain and snow. In general, the DPR onboard the GPM can provide more detailed information on microphysics and better accuracy in rainfall estimation from dual-wavelength radar measurements.

Three scanning modes were included in DPR (Hou et al., 2014; Iguchi et al., 2017). For normal scan (NS), the scan pattern is similar to that of TRMM PR, which has 49 footprints in a scan. The footprint size is approximately 5 km in diameter. In the matched scan (MS), the beams are matched to the central 25 beams of Ku-band footprints, providing a swath of 120 km. The high-sensitivity scan (HS) Ka-band footprints were interlaced with Ku-band footprints and had 24 angle bins. The range resolution of the NS and MS measurements was 250 m. The range resolution was 125m for HS measurement because the radar echoes were oversampled at twice the rate. The minimum rainfall rate is 0.2 mm/h for Ka-band of DPR and 0.5 mm/h for Ku-band. This study used DPR Level-2A products (2ADPR) based on dual-wavelength information. Three modes of 2ADPR products, 2ADPR-NS, 2ADPR-MS, and 2ADPR-HS, were used. It should be noted that the inner swath (footprints 13–37) of 2ADPR-NS is the same as that of 2ADPR-MS. The key variables used in this study include zFactorCorrected, PrecipRate, paramDSD, heightBB, typePrecip, and phase.

2.2 CDP data

Dual-polarization weather radar is a type of radar that can transmit and receive both horizontal and vertical polarization waves. Only three basic data, including radar reflectivity

factors (Z), radial velocity, and velocity spectrum width, can be obtained using conventional single-polarization radar. More parameters can be measured from the dual-polarization radar, such as differential reflectivity (Z_{DR}), differential propagation phase (ϕ_{DP}), specific differential phase shift (K_{DP}), and cross-correlation coefficient (ρ_{hv}). Compared with conventional weather radar, dual-polarization radar has notable advantages in identifying different hydrometeor types and retrieving DSD parameters (Bringi et al., 2001). Moreover, the polarization parameters were relatively insensitive to variations in the DSD. Therefore, the accuracy of quantitative precipitation estimation can be further improved using dual-polarization radar measurements. Data from the CDP at Nanjing University of Information Science and Technology were used in this study. The wavelength of the CDP is 5.3 cm, and the beam width is 0.54 degrees. The radar has a range resolution of 75 m, with a coverage of 144 km. During the precipitation operation mode, the CDP conducts a volume coverage pattern with 14 elevation scans. For one volume scan, the CDP typically takes approximately 7–8 min. Before application, the measured data of CDP is quality controlled with a series of preprocessing (Kou et al., 2018), such as recognition and removal of ground clutter with a fuzzy logic algorithm, median filtering of K_{DP} and Z_{DR}, and the attenuation correction of radar reflectivity at horizontal polarization (Z_h) with the K_{DP}-Z_h joint correction method (Park et al., 2005).

2.3 Hydrometeor identification

Dual-polarimetric radar measurements are sensitive to hydrometeors' type, shape, and size distribution in a resolution volume. Classifying hydrometeors is important for optimizing the rainfall retrieval algorithm and evaluating the assumptions made in the rainfall retrieval processes. The hydrometeor identification will be utilized following optimization of rainfall retrieval with different hydrometeor classes and rainfall comparison between DPR and CDP for different phases. Currently, the algorithms frequently used for hydrometeor identification are, in general, based on the fuzzy logic approach. Fuzzy logic classification generally has three steps: fuzzification, aggregation, and defuzzification. In this study, we use a fuzzy logic algorithm similar to the scheme in Park et al. (2009) but in a simplified manner. This module applies three radar measurements, Z_h, Z_{DR}, and ρ_{hv}, as the input; the weighting functions were assumed to be 1. Ten classes of radar echo were identified as the output: ground clutter or anomalous propagation (GC/AP), biological scatterers (BS), dry aggregated snow (SW), wet snow (WS), crystals (CR), graupel (GR), big drops

(BD), light and moderate rain (RA), heavy rain (HR), and a mixture of rain and hail (HA). Some restrictions were set according to the location of the melting layer (Schuur et al., 2003).

2.4 Optimization of rainfall retrieval

Dual-polarization radar can provide both back-scatter and differential propagation phase information. Thus, it can constrain the uncertainty of quantitative rainfall estimation resulting from DSD variations. The parameters Z_h, Z_{DR}, and $K_{DP,}$ are typically used either alone or in combination to estimate rainfall (Chen et al., 2017; Cifelli et al., 2011), such as the relationships of $R(Z_h)$, $R(Z_h, Z_{DR})$, and $R(K_{DP})$, where R indicates the rainfall rate. Each rainfall relationship has its advantages and disadvantages. No standard criterion can be applied to determine the optimal estimator for a given set of dual-polarization measurements. In this study, the rainfall estimators were combined. The most appropriate rainfall relation was selected based on the hydrometeor classification and logistic regression algorithm. First, the rainfall estimators of $R(Z_h)$, $R(Z_h, Z_{DR})$, and $R(K_{DP})$ were established through the disdrometer data in the Nanjing area using a neural network algorithm. Then, particular rainfall estimators were selected for the liquid samples determined by the hydrometeor identification results. A logistic regression model was built based on the CDP rainfall retrieved from the rainfall estimators and spatial-temporal matched rain gauge data. During logistic modeling, we randomly selected a part of the data for training and the other part for testing. The optimization selection of rainfall estimators was performed for the liquid samples according to the established logistic model.

Figure 1 shows the scatter plots of rainfall from the rain gauge and CDP with different rainfall algorithms. The data are from all precipitation events that CDP matched with DPR during 2015–2017. Figure 1a-c shows the scatter plot of rain gauge data and CDP rainfall with individual rainfall estimators of $R(Z_h)$, $R(Z_h, Z_{DR})$, and $R(K_{DP})$. The optimization retrieval algorithm obtained the rainfall from the CDP in Figure 1d. The statistical indices for quantitative comparisons are shown in Figure 1, where CC is the correlation coefficient, and Bias is the mean bias of the data on the y-axis minus the data on the x-axis. MAE is the mean absolute error that measures the average magnitude of the error, and RMSE is the root mean square error. From Figure 1, it is seen that $R(K_{DP})$ is noisy at low rainfall rates but is good at high rainfall rates. $R(Z_h)$ and $R(Z_h, Z_{DR})$ do not work well in heavy rain but perform well in light rain. The results of the optimization retrieval algorithm were in good agreement with the rain gauge data, and the correlation coefficient reached

approximately 0.83. The bias decreased to -0.19 mm/h. The optimization retrieval algorithm considers the hydrometeor type and the rainfall estimation performance of different rainfall estimators, which provide superior rain estimates for a given set of polarimetric variables. The optimization of rainfall retrieval result of the CDP will be used for later rainfall comparison with DPR.

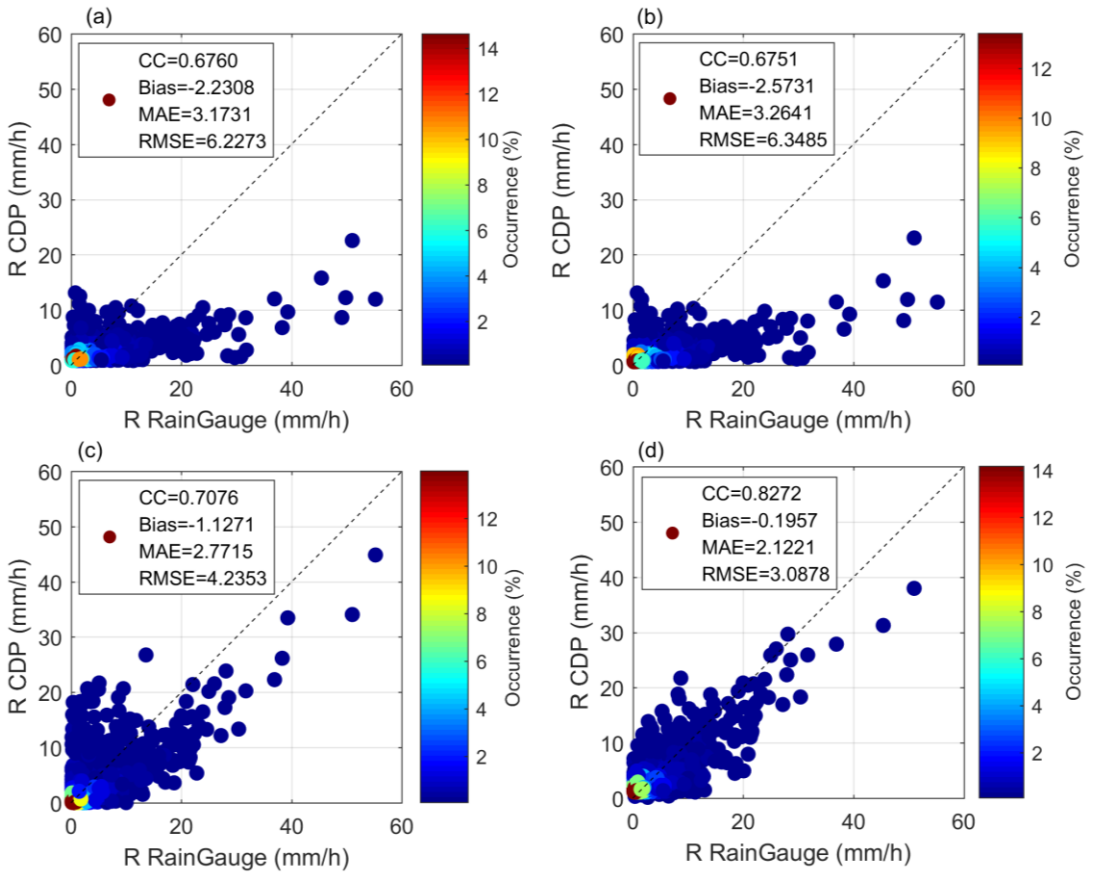

Figure 1. Scatter density plots of rainfall rate obtained by different rainfall retrieval algorithms of CDP and rain gauge. (a) $R(Z_h)$, (b) R (Z_h, Z_{DR}), (c) $R(K_{DP})$, and (d) optimization of rainfall retrieval.

2.4 D_m retrieval

The mass-weighted mean diameter D_m is one of the DSD parameters that are especially important for rainfall estimation. The V05 version of the DPR level-2 algorithm assumes constraint relationships between the rainfall rate R and D_m, namely, $R(D_m)$. To better understand the rainfall comparisons from DPR and CDP, D_m comparisons were introduced. D_m was estimated from the CDP using a variational retrieval approach (Chen et al., 2021). A variational method utilized forward observation operations that converted state variables into observations. The D_m and liquid

water content W were state variables, and Z_h, Z_{DR}, and K_{DP} were observations. After establishing the forward model, the optimal D_m and W estimates were obtained using the nonlinear iteration to minimize the cost function. The variational retrieval method considers the uncertainty of the DSD and measurement error, which can produce an improved D_m estimate. The D_m estimate from the dual-polarization radar can also be obtained by an empirical relationship between D_m and Z_{DR} based on DSD data from a disdrometer. To demonstrate the reliability of the D_m estimate from the CDP, the retrieved D_{m} was compared with the D_m from the calculation result of the disdrometer data with scatterplot and time sequence diagram. Figure 2a comprise the D_m estimate from CDP and D_m calculated from the disdrometer data available for 2015, where the disdrometer is at atmospheric comprehensive observatory of Nanjing University of Information Science and Technology. The data in Figure 2b is from a time series of 3:00 to 14:00 UTC on August 10, 2015. As shown in Figure 2, the retrieved D_m with the variational algorithm was consistent with the D_m calculated from the disdrometer, and the correlations were above 0.85. The D_m-Z_{DR} method produced an underestimation at a larger D_m. The variational retrieval results for D_m were selected in this study.

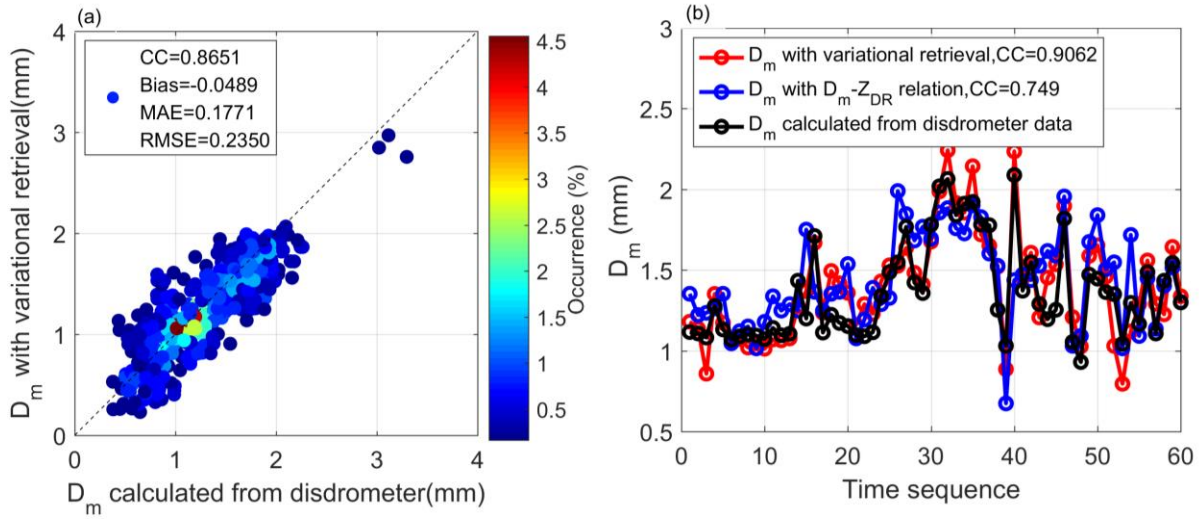

Figure 2. Comparison between D_m estimated with variational approach and D_m calculated from disdrometer. (a) Scatter density plot. (b) Time sequence diagram.

3 Results and discussion

3.1 Comparison of BB height and phase recognition

Accurate depiction of the BB is important for rain type classification and phase identification of the DPR. Before evaluating the DPR reflectivity measurements and rainfall products of different types and phases, the BB height estimation from DPR and CDP was first compared. The BB appears near 0°C and returns a strong echo at the radar measurement. The detection of BB for DPR is involved in the classification (CSF) module. A dual-frequency ratio (DFR) method was used to detect BB (Iguchi et al., 2017). Then, the height of the BB was obtained by searching the BB reflectivity peak height. In this study, we extracted DPR BB height data directly from the 2ADPR product of the heightBB variable. For CDP, BB detection was performed using a fuzzy logic algorithm. The height of the BB was calculated assuming an equivalent Earth radius to account for standard beam refraction (Cao et al., 2018).

Figure 3 shows a scatter plot of the BB height from CDP and 2ADPR. Among the 17 matching cases with extensive stratiform regions, the DPR NS and MS modes recognized the BB of 17 cases, consistent with CDP. In comparison, the DPR HS mode only recognized the BB of 10 cases. In the case of the HS mode at the Ka-band, the BB peak may not be clear, and the peak position of Ka-band may be displaced from that of the Ku-band (Iguchi et al., 2017, Le & Chandrasekar, 2013). As shown in Figure 3, the differences in BB height from the CDP and DPR NS and MS modes were very small, and the correlation coefficients for the NS and MS modes were more than 0.9. The statistical comparison results for the BB height are presented in Table 1. The MAE and RMSE for the NS and MS modes were less than 0.2 km. The slight difference in BB height detection between the DPR and CDP may be mainly due to the scanning types and sampling differences.

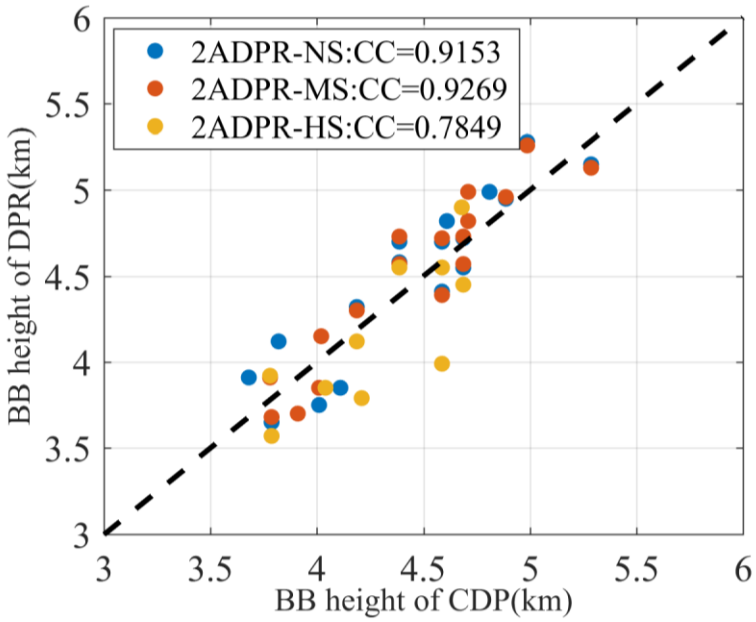

Figure 3. Comparison of BB height from CDP and DPR with NS, MS, and HS scanning modes. The blue, red, and orange colors represent NS, MS, and HS modes, respectively.

Table 1 Statistical comparison of BB height from CDP and DPR

	CC	Bias	MAE	RMSE
2ADPR-NS	0.9153	0.0561	0.1764	0.1927
2ADPR-MS	0.9269	0.0508	0.1623	0.1792
2ADPR-HS	0.7849	-0.1242	0.2288	0.278

Precipitation type classification and hydrometeor phase state detection are two critical aspects of the microphysical retrieval algorithm of DPR. In addition to the BB height comparison, the hydrometeor phase recognition of DPR was also validated with the ground dual-polarization radar. High-resolution measurement and dual-polarization capability make the CDP prominent in distinguishing between different hydrometeor types. Eight classes of hydrometeors were identified in the CDP using the fuzzy logic algorithm presented in Section 2.3. For DPR, the dual-frequency ratio (DFR) profile was used to distinguish the frozen, mixed-phase, and liquid regions (Le et al., 2016). In this study, we divided the matched samples into liquid and non-liquid particles based on the hydrometeor identification results from the CDP. The large drops and light, moderate, and heavy rain determined by CDP were classified as liquid samples. The other hydrometeors were classified as non-liquid samples. In a matched volume of CDP, a particular hydrometeor type with the highest volume is regarded as the final sample type.

The conditional probability of liquid and non-liquid phase identification of DPR for all samples is summarized in Table 2; it was defined as the ratio of the number of samples identified as a certain phase by both DPR and CDP to the number of samples identified as a certain phase by CDP. Conditional probability of the liquid phase for the three scanning modes was more than 95%. Conditional probability of non-liquid identification for the NS mode was slightly worse than that of the liquid phase. However, the conditional probability of non-liquid identification of the HS mode was low, indicating a large difference for non-liquid identification from CDP and DPR HS. For the DPR HS mode, the DF method was also used by interpolation (Iguchi et al., 2017). For non-liquid samples, the vertical resolution of the CDP becomes coarse as the range increases. Data re-sampling could contribute to large differences in DPR and CDP hydrometeor identification. The BB height and phase identification agreed well between the CDP and DPR NS and MS modes, and the agreement for the HS mode was slightly worse.

Table 2 Conditional probability of liquid and non-liquid phase identification of DPR

Scanning modes	Liquid	Non-liquid
DPR NS	95.34%	90.38%
DPR MS	95.41%	95.55%
DPR HS	97.69%	78.97%

3.2 Comparison of reflectivity

Radar reflectivity is a fundamental product used to retrieve rainfall from radar data. Before proceeding to comparisons of rainfall, we considered comparisons of reflectivity measured by DPR and CDP. Owing to the attenuation of reflectivity in C-band measurements, a K_{DP}-Z_h joint correction method was used to correct the attenuation of the reflectivity of CDP (Park et al., 2005). The attenuation correction was evaluated via comparison with the reflectivity from the S-band radar at Longwangshan, which is close to the CDP. The figures for attenuation correction evaluation are not shown here. The volume matching method, used for comparison, was performed at each geometric intersection of the DPR and CDP beams by averaging the data samples within the volume (Bolen & Chandrasekar, 2003). The matching method minimized the error due to re-sampling.

Volume-matched reflectivity from CDP was compared with attenuation-corrected reflectivity from 2ADPR-NS, 2ADPR-MS, and 2ADPR-HS. The minimum detectable signal was

approximately 12 and 18 dBZ for the DPR Ka- and Ku-bands. To improve the matching effect, the threshold value of CDP was set to 18 dBZ when matching the DPR NS and MS modes and 12 dBZ when matching the DPR HS mode. Figure 4 shows the reflectivity scatter density plots of the CDP and DPR in the NS, MS, and HS modes for stratiform and convective samples. The precipitation type was noted according to the typePrecip product of DPR. The first, second, and third columns of Figure 4 show scatter density plots between CDP reflectivity and 2ADPR-NS, 2ADPR-MS, and 2ADPR-HS reflectivity, respectively. The first, second, and third rows of Figure 5 represent the reflectivity comparison for all, stratiform, and convective samples, respectively.

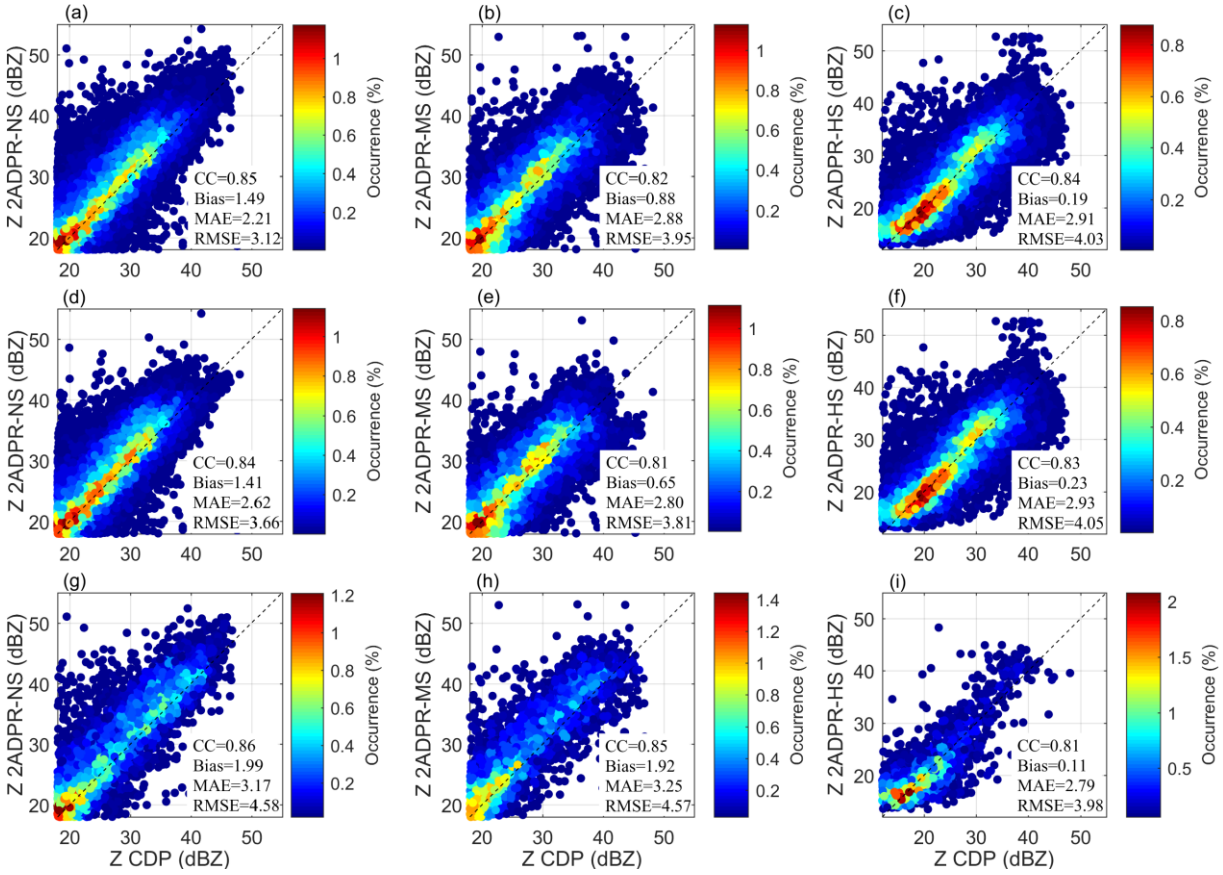

Figure 4. Scatter density plots of volume matched reflectivity between CDP and DPR NS, MS, and HS modes for different precipitation types. (a-c) All NS, MS, and HS data samples. (d-f) Stratiform samples for NS, MS, and HS data. (g-i) Convective samples for NS, MS, and HS data.

From Figure 4, we can see that the agreement was good for all the DPR scanning modes, and the CCs were more than 0.8 for both stratiform and convective precipitation. The NS mode showed the best agreement for both stratiform and convective precipitation. The CCs were higher for convective precipitation for the NS and MS modes than for stratiform precipitation. However, the

MAE and RMSE were smaller for stratiform precipitation. The bias for convective precipitation for the NS and MS modes was approximately 1.9 dB, consistent with the band difference between the C-band and Ku-band (Liao & Meneghini, 2009). The number of convective samples was small for the HS mode, and the bias was much smaller than that of the NS and MS modes. Thus, the reflectivity observed in the HS mode is lower, and its capability to detect convective precipitation is relatively weak. Nevertheless, the reflectivity measurement of the DPR HS was consistent with the CDP measurement overall.

To further demonstrate the influence of the hydrometeor phase, reflectivity data were compared based on the hydrometeor types of CDP. Cao et al. (2013) revealed that the reflectivity could be 2 dB higher in the Ku-band than that of the S-band for rain measurements in the range of 40–50 dBZ, owing to the different back-scattering cross-sections measured by the radars at different bands. The different types of hydrometeors have different back-scattering cross-sections at different radar bands, resulting in reflectivity measurement discrepancies. In the current study, we performed theoretical simulations of radar reflectivity factors to better explain the reflectivity comparisons between DPR and C-band ground radar. The radar reflectivity factor *Z* is given by

$$Z = \frac{\lambda^4}{\pi^5 |K|^2} \int_0^\infty N(D)\sigma(D,\lambda)dD \tag{1}$$

where is λ the radar wavelength, $|K|^2$ is the dielectric constant of water, *D* is the effective particle diameter, $\sigma(D,\lambda)$ is the back-scattering cross-section, and *N*(*D*) is the particle size distribution (PSD). Here, the normalized three-parameter (N_w, D_m, μ) gamma PSD model is used in the simulation:

$$N(D) = N_w \frac{6(\mu+4)^{\mu+4}}{4^4\Gamma(\mu+4)} \left(\frac{D}{D_m}\right)^\mu \exp\left(\frac{(\mu+4)D}{D_m}\right) \tag{2}$$

The parameter settings in the gamma PSD model for different hydrometeors are similar to those in (Cao et al., 2013). The back-scattering cross-section of hydrometeors was derived from the T-matrix calculation. Here, we introduce the DFR to quantify the scattering differences between the two frequencies:

338
$$DFR_{C-Ku} = 10\log_{10} Z(C) - 10\log_{10} Z(Ku)$$
$$DFR_{C-Ka} = 10\log_{10} Z(C) - 10\log_{10} Z(Ka) \quad (3)$$

339 The DFRs between the C-band and Ku- and Ka-band for different hydrometeors are shown
340 in Figure 5. For liquid water, the simulated reflectivity differences were concordant with the results
341 reported by Wen et al. (2011). Beyond 40 dBZ, the Ku-band reflectivity can be 2 dBZ higher. In
342 contrast, the Ka-band reflectivity can be 4 dBZ lower than that of the C-band. For non-liquid
343 hydrometeors, the DFR is positive because of the non-Rayleigh scattering effect when the
344 reflectivity increases above 30–40 dBZ. Owing to the more serious non-Rayleigh scattering effect
345 for the Ka-band, the DFR between the C and Ka-bands was much larger than that of the Ku-band.

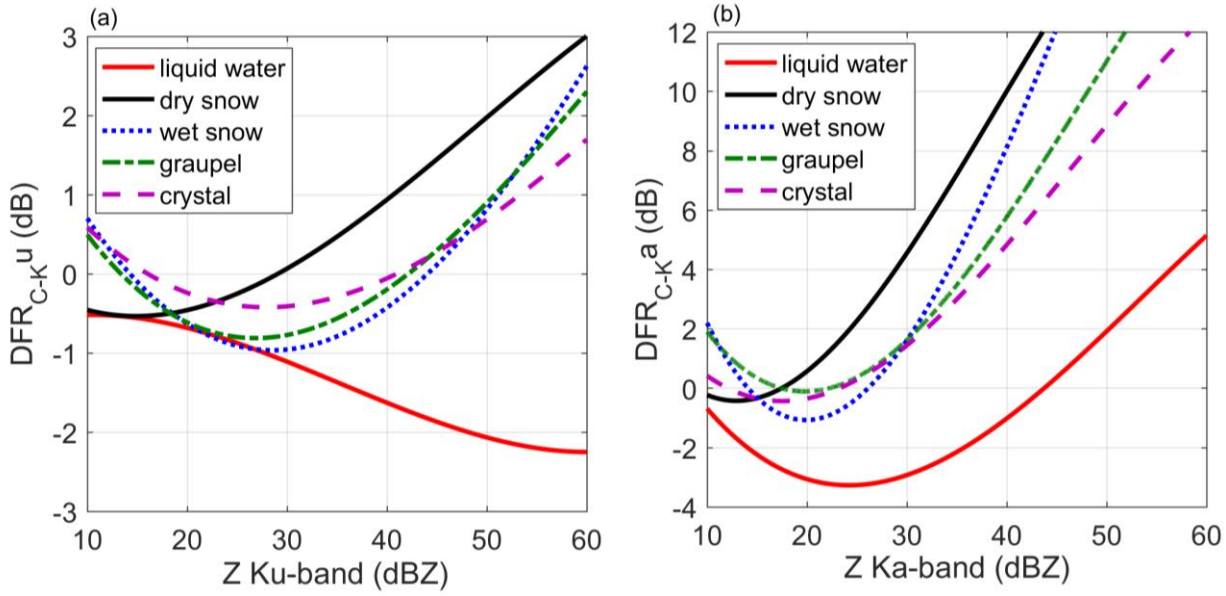

346
347 **Figure 5.** DFR between reflectivity factors at C-band and Ku- and Ka-band for different hydrometeors. (a) DFR
348 between C- and Ku-band. (b) DFR between C- and Ka-band.

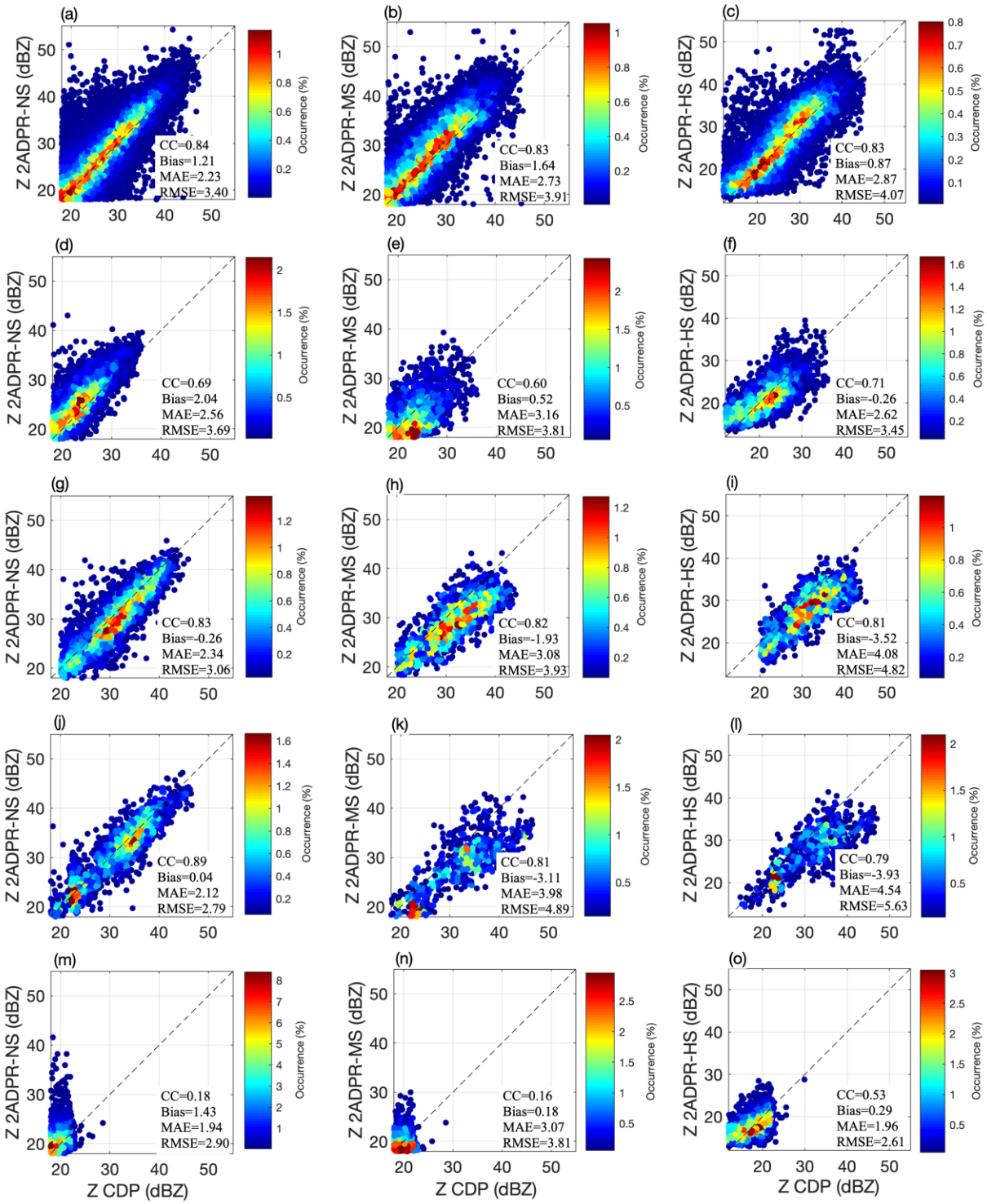

Figure 6. Scatter density plots of volume matched reflectivity between CDP and DPR NS, MS, and HS modes for different hydrometeor types. (a-c) Liquid samples. (d-f) Dry snow. (g-i) Wet snow. (j-l) Graupel. (m-o) Crystal.

Figure 6 shows the scatter density plots of reflectivity measurements between CDP and DPR for different hydrometeor types obtained by CDP hydrometeor classification. The first,

second, and third columns of Figure 6 show scatter density plots between CDP reflectivity and 2ADPR-NS, 2ADPR-MS, and 2ADPR-HS reflectivity, respectively. The first, second, third, fourth, and fifth rows of Figure 6 represent the reflectivity comparison for liquid, dry snow, wet snow, graupel, and crystal samples. Very few heavy rain samples were identified, and no mixture of rain and hail samples was identified. The liquid samples mainly included big drops and light and moderate rain. The liquid samples agreed well with the three scanning modes. An obvious positive bias existed in the NS and MS modes, consistent with the simulated results shown in Figure 5. The scatterplots of wet snow and graupel show obvious negative biases in the HS mode. The bias was small for the NS mode, consistent with the expectations shown in the simulated results of Figure 5. The consistency of dry snow for the three scanning modes was slightly worse, and the comparison results did not agree with the simulations. One possible reason is that the geometry of dry snow observed by dual-polarization radar is different in the horizontal and vertical directions, resulting in the deviation of the reflectivity factor; another reason may be that the complex geometry of dry snow makes the Mie scattering simulation results different from the actual situation, resulting in a small amount of band correction. The scatterplots of the crystal show that they are almost irrelevant between CDP and DPR for NS and MS modes, which may be specific or perhaps indicate a poor capability for crystal measurement of DPR NS and MS. However, the consistency of the crystal for the HS mode was improved, and this may partially demonstrate that the high sensitivity of the Ka-band is beneficial for crystal measurement. Overall, the reflectivity comparison for different hydrometeor types is consistent with the simulation results, except for the measurement of crystal samples.

3.3 Comparison of rainfall

3.3.1 Comparison of rainfall for liquid samples

Volume matched samples of instantaneous rainfall products from DPR with NS, MS, and HS modes were compared against rainfall from CDP with the optimization retrieval algorithm in Section 2.3. The DPR products used in this study were the 2ADPR products retrieved using a DF algorithm. The DF algorithm was executed for the pixels of all three scanning modes. In the DF algorithm, pixels in the inner swath of the NS mode are categorized as dual-beam (DB) pixels, and the other pixels are categorized as single-beam (SB) pixels. The DB pixels in the DF algorithm can produce DSD information; therefore, the rainfall estimate can be improved. For SB pixels, the

DF algorithm can use data from DF observations at neighboring pixels (Iguchi et al., 2017). The DF algorithm can provide better rainfall estimates at SB pixels using the characteristics of the DSD estimated by DF measurements at DB pixels.

Figure 7 shows the scatter density plots between the matched liquid samples of CDP rainfall and 2ADPR rainfall products with NS, MS, and HS scanning modes. A minimum threshold of 0.1 mm/h, and a maximum threshold of 60 mm/h, was set for both CDP and DPR rainfall intensity. The V05 version of the DPR rainfall algorithm assumes constraint relationships between the rainfall rate R and D_m. The D_m values were also compared, as shown in Figure 8. The samples were again classified according to the precipitation type. The first rows of Figures 7 and 8 indicate scatter plots of all matched samples, and the second and third rows indicate stratiform and convective samples. The first, second, and third columns represent the NS, MS, and HS modes, respectively.

From Figure 7, it is seen that the comparison performances of NS, MS, and HS are similar for all liquid samples, with a correlation of approximately 0.58 and MAE of approximately 3.3 mm/h. For the NS and MS modes, there is a slight underestimation for light rain and an overestimation for heavy rain compared with the CDP rainfall estimation. This might be partially due to the underestimation of the CDP in heavy rain, as shown in Figure 1. Although optimization retrieval has been performed for CDP and the overall performance is optimal compared with the rain gauge data, the CDP rainfall is slightly underestimated in heavy rain. Another reason may be that D_m is overestimated at large particle sizes, as shown in Figure 8a-b. For HS mode, the mean bias is -1.13 mm/h, which means that the rainfall estimates of HS are low compared to those of NS and MS modes. The comparative performance of stratiform samples improved compared to all samples, and the correlation coefficients increased. The correlation of HS mode for stratiform precipitation reached 0.63, and the mean bias was about -0.15 mm/h, which showed the best agreement with CDP estimation. This proves that the HS mode has advantages in the estimation of stratiform precipitation and light rain. However, the HS mode shows poor performance for convective samples. Although the CC was only 0.38, the reflectivity comparison showed good agreement. Affected by the band, the HS mode is not suitable for estimating convective precipitation and heavy rain. The MS mode showed the best performance in convective rainfall estimation, with CC of 0.66 and MAE of 3.02 mm/h. Many factors may affect the rainfall estimation performance in convective cases, such as DSD variation, attenuation error, and non-

uniform beam filling. The MS mode can utilize the DF method to obtain relatively accurate DSD and attenuation parameters, making the MS mode perform well in convective precipitation. The CC, MAE, and RMSE of the NS mode are slightly worse than those of the MS mode in convective precipitation, which may be because the pixels in the outer swath of NS belong to the SB pixels.

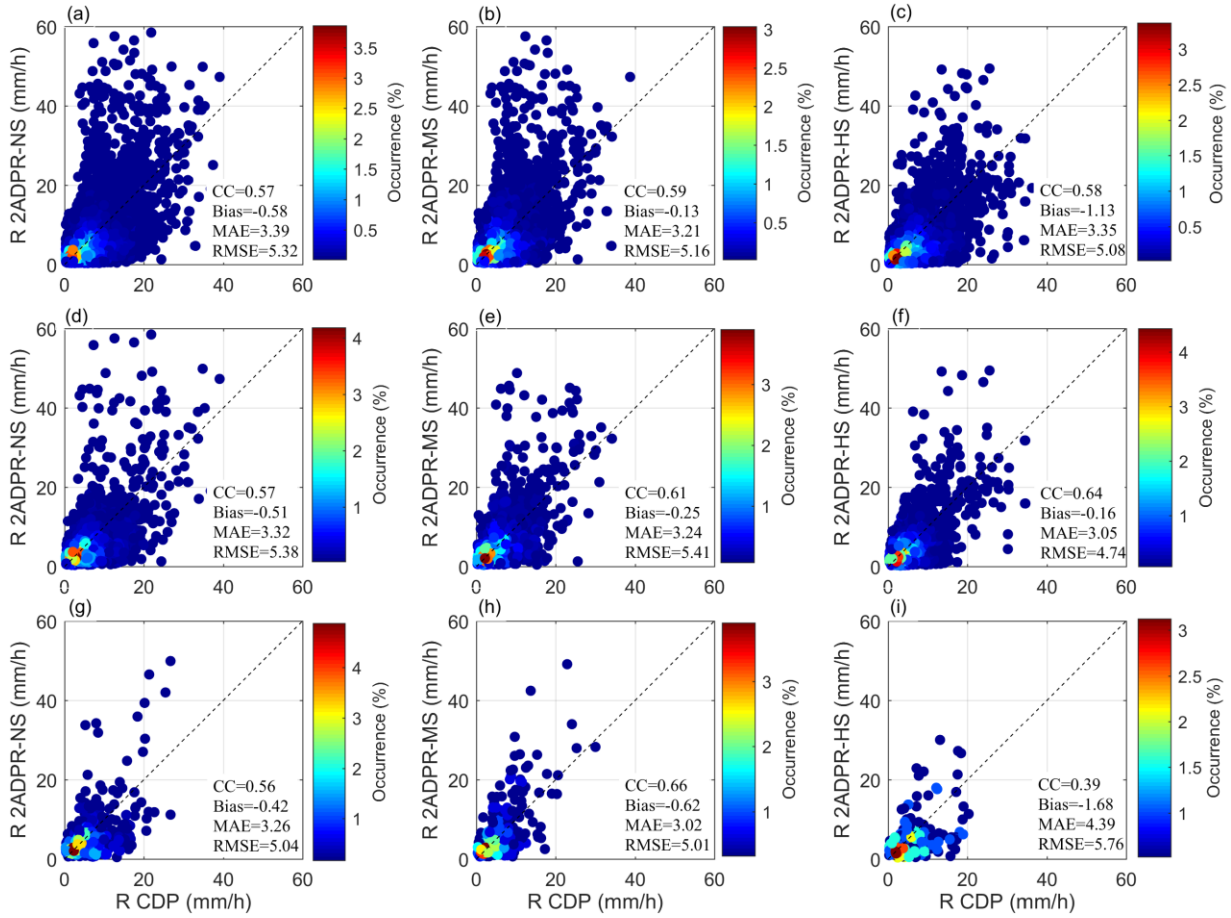

Figure 7. Scatter density plots of volume matched rainfall between CDP and DPR NS, MS, and HS for liquid precipitation. (a-c) All NS, MS, and HS data samples, (d-f) Stratiform samples for NS, MS, and HS data, (g-i) Convective samples for NS, MS, and HS data.

D_m is one of the two DSD parameters used in estimation of the DPR, important for rainfall estimation. To better understand the rainfall estimation and identify conditions that affect the goodness of the estimation, D_m comparisons are shown in Figure 8. From Figure 8, we can see that the DPR NS and MS scan modes show good agreement of D_m with CDP for both stratiform and convective precipitation, and the MAE is within 0.25 mm. Relative to the NS mode, the consistency of D_m for the MS mode is better, which can partially explain the better agreement of rainfall estimation of the MS mode. Z and D_m are extremely important factors that influence the rainfall estimation of DPR. In Figure 6, we can see that the Z measurements of the NS and MS

modes are similar for the liquid samples, and the agreement for the MS mode is slightly worse than that of the NS mode. Nevertheless, the MS mode showed advantages in convective rainfall estimates concerning the NS mode, thereby verifying the importance of DF measurement for DSD retrieval and rainfall estimation. The HS mode had a relatively worse result for the D_m comparison, and it exhibited an upper limit of D_m at 3 mm. The threshold of D_m of HS is related to the setting of the DPR HS retrieval algorithm (D'Adderio et al., 2018; Iguchi et al., 2017). Despite the D_m problem, the HS showed good agreement with stratiform rainfall estimates.

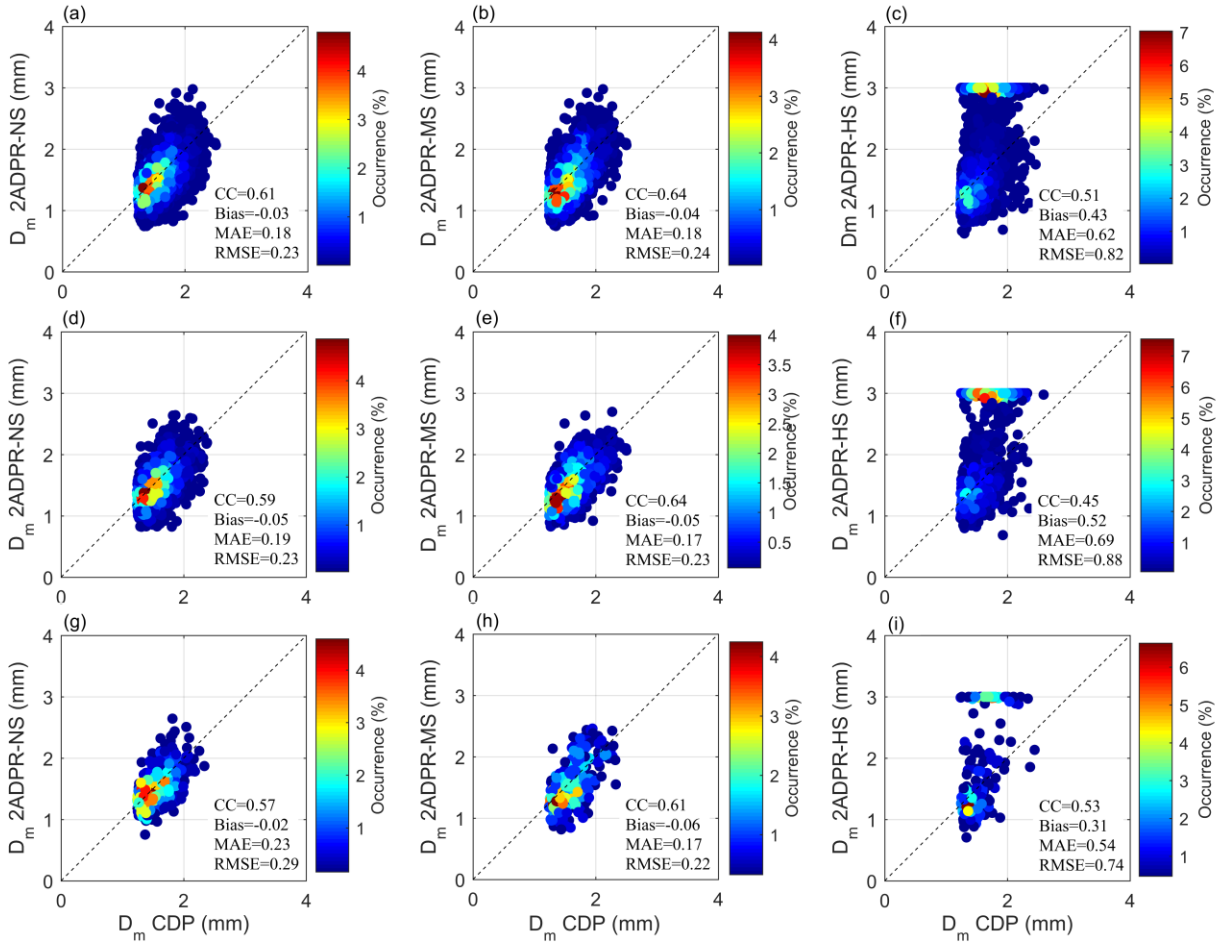

Figure 8. Scatter density plots of volume matched D_m between CDP and DPR NS, MS, and HS modes for liquid precipitation. (a-c) All NS, MS, and HS data samples. (d-f) Stratiform samples for NS, MS, and HS data. (g-i) Convective samples for NS, MS, and HS data.

3.3.2 Comparison of rainfall for non-liquid samples

The liquid precipitation products of DPR can be evaluated using ground-based radars, rain gauges, and disdrometers (Chen et al., 2017; Lasser et al., 2019; Radhakrishna et al., 2016),

whereas it is relatively difficult to compare and validate non-liquid precipitation. Non-liquid particles are usually far from ground-based radar. They have a poor spatial matchup with surface precipitation estimation. However, there is no suitable measured PSD data to fit the rainfall relations of non-liquid precipitation. In 3D precipitation, a large number of particles are non-liquid samples. It is necessary to cross-validate the rainfall estimation of non-liquid samples between DPR and ground-based dual-polarization radar.

Owing to the lack of measured PSD data, we developed the radar rainfall relations of non-liquid particles based on theoretical simulations, which assumed appropriate scattering and microphysical models. From Figure 6, it is seen that the scatters of the crystal are almost irrelevant for the DPR NS and MS modes. Thus, the crystal samples are not considered. The *Z*-*R* relations for non-liquid hydrometeors, including dry snow, wet snow, and graupel, were obtained from simulations. The scattering amplitudes were computed using the T-matrix method. The *Z* calculation and PSD model are based on formulas (1) and (2). The rainfall rate *R* can be calculated by

$$R = \int_0^\infty N(D)M(D)v(D)dD \tag{3}$$

where $M(D)$ is the mass of a particle with D and $v(D)$ is the terminal fall velocity. $v(D)$ can be calculated as follows (Brandes et al., 2002):

$$v(D) = -0.1021 + 4.932D - 0.9551D^2 + 0.07934D^3 - 0.002362D^4 \tag{4}$$

The fitted rainfall relations for dry snow, wet snow, and graupel are as follows:

$$\begin{aligned} R &= 0.0392Z^{0.6968} \ (dry\,snow) \\ R &= 0.0201Z^{0.6538} \ (wet\,snow) \\ R &= 0.0183R^{0.6752} \ (graupel) \end{aligned} \tag{5}$$

where Z is in mm^6/m^3 and R is in mm/h.

Figure 9 shows the simulated rainfall relation of dry snow, wet snow, graupel, and corresponding *Z*-*R* relations in Giangrande et al. (2008), as well as the *Z*-*R* relation obtained in Section 2.4 from the measured DSD data of rain. The simulated rainfall relations (red lines) for dry snow and graupel are similar to those in Giangrande et al. (2008) (blue dashed lines), and their differences are small. The black dotted dashed lines represent the rainfall relations obtained from

the DSD data from the disdrometer for liquid precipitation. The differences between the red and black lines were significant, which again proved the microphysical difference of liquid and non-liquid hydrometers. We will use the simulated rainfall relations to estimate CDP rainfall estimation for non-liquid hydrometers.

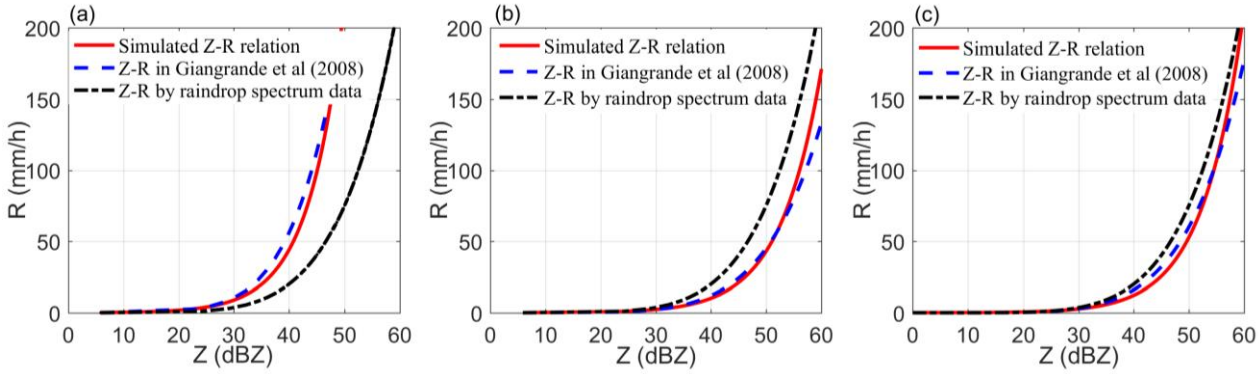

Figure 9. Comparisons of *Z-R* relations with different methods for non-liquid hydrometeors. (a) Dry snow. (b) Wet snow. (c) Graupel.

Figure 10 shows the scatter density plots between matched samples of CDP rainfall obtained by simulated rainfall relations and 2ADPR rainfall products for dry snow, wet snow, and graupel with NS, MS, and HS scanning modes. The CDP hydrometeor classification determined the hydrometeor types. The first, second, and third rows of Figure 10 indicate the scatter plots of matched samples for dry snow, wet snow, and graupel samples, respectively. The first, second, and third columns represent the DPR NS, MS, and HS modes, respectively. We can see that the rainfall rates of the dry snow, wet snow, and graupel from DPR are consistent with those recorded via CDP on the whole, and the bias are within 0.8 mm/h for all scanning modes. A slight overestimation in the DPR estimate exists, especially for the NS and MS modes, which may be related to the rainfall algorithm of DPR. An R-D_m relation is used for the entire atmospheric column in the DPR algorithm, regardless of whether the gates are classified as liquid or solid (Chase et al., 2020). The only difference between liquid and solid phase retrieval is the complex refraction index and $v(D)$ (Iguchi et al., 2017). The correlation coefficient of non-liquid precipitation estimation for the NS mode is the highest, which is partially explained by the best agreement of reflectivity comparison of the NS mode. The agreement of the HS mode is slightly worse than that of the NS mode. Despite the high sensitivity, the HS mode shows no apparent advantage in the non-liquid rainfall estimation of snow and graupel, which may be related to its low conditional probability of non-liquid hydrometeor identification. For the three types of non-liquid hydrometeors, the MAE

for dry snow for the three scanning modes was between 1 and 1.4 mm/h, the MAE for wet snow was approximately 2 mm/h, and the MAE for graupel varied in the range 2.3–3 mm/h. Due to the complex physical properties of wet snow and graupel, rainfall relation simulations are difficult, resulting in errors. The difference between DPR and CDP rainfall estimation for graupel is obvious when the rainfall is above 10 mm/h. However, the reflectivity comparisons of graupel samples for the three scanning modes show good agreement. The large difference in rainfall estimation of the graupel may be related to the DPR rainfall algorithm. Comparing Figures 7 and 10, it is seen that in general, the agreement of rainfall estimation of liquid precipitation is better than non-liquid precipitation. The physical characteristics of liquid and non-liquid hydrometeors are different. There are no special rainfall relations for non-liquid precipitation for DPR. Due to the lack of measured PSD data, rainfall retrieval via ground radar for non-liquid precipitation is also difficult. The improvement of the rainfall algorithm for non-liquid hydrometeors is necessary for both DPR and ground dual-polarization radar.

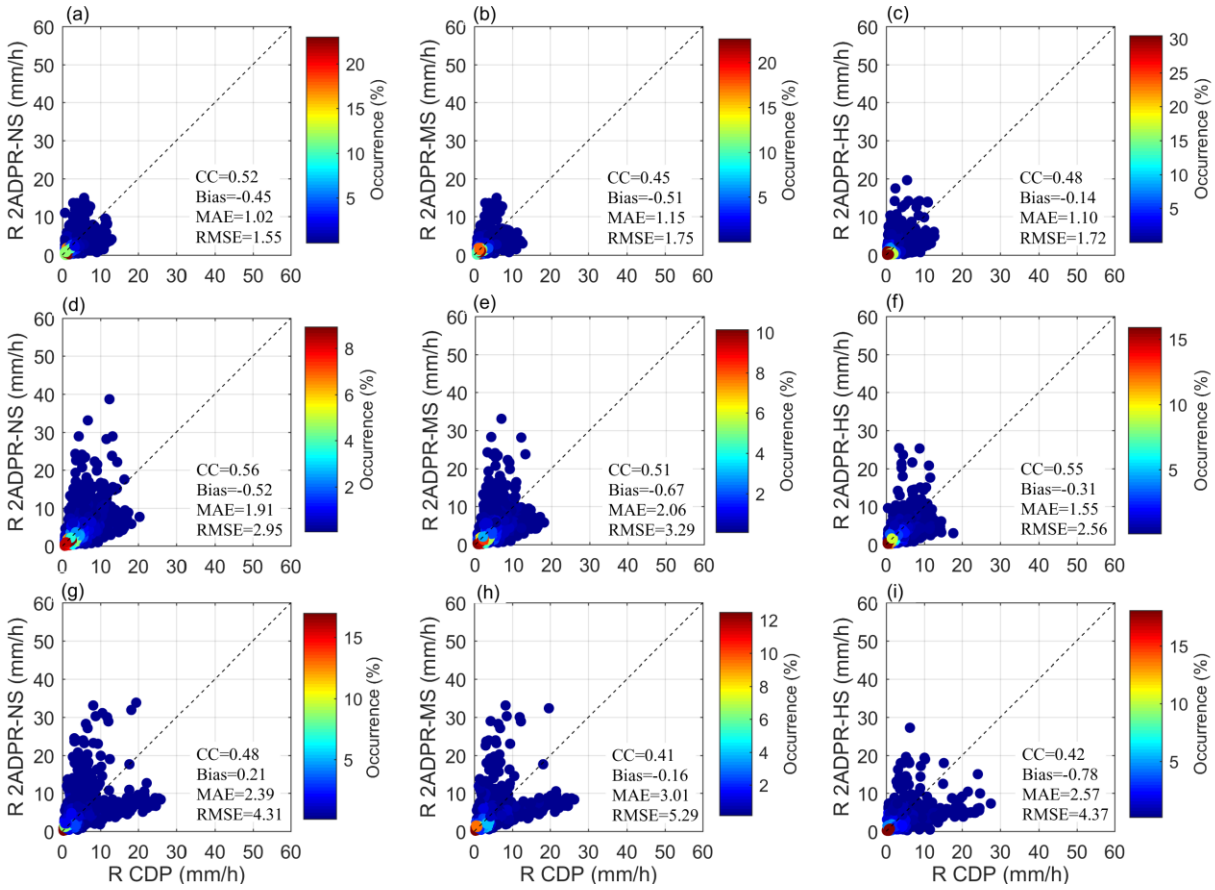

Figure 10. Scatter density plots of volume matched rainfall between CDP and DPR NS, MS, and HS modes for snow and graupel. (a-c) Dry snow samples for NS, MS, and HS. (d-f) Wet snow samples for NS, MS, and HS. (g-i) Graupel samples for NS, MS, and HS.

5 Conclusions

The combination of hydrometeor classification and DSD parameter retrieval of dual-polarization radar is of great interest for the cross-validation of DPR rainfall retrieval. The 3D rainfall data from the CDP and DPR NS, MS, and HS modes were compared for different precipitation types and precipitation phases. To better explicate the rainfall products, comparisons of the BB, reflectivity, and DSD parameter of D_m were performed. The main conclusions are as follows.

1) The comparison of the BB revealed that the correlation coefficients for the NS and MS modes are greater than 0.9. The consistency of the HS mode is relatively worse, which may be due to its unclear BB peak. The conditional probability of liquid phase identification by DPR, with respect to CDP, exceeded 94%. In comparison, it was only 78% for the non-liquid phase identification of the DPR HS mode.

2) The agreement of reflectivity for the three modes of DPR is good for both stratiform and convective precipitation, with correlation coefficients greater than 0.81 and bias within 1 dB. By comparing reflectivity associated with different hydrometeor types, the differences among hydrometeor types conform to the scattering simulation for different bands, except for the crystal. The agreement of the crystal in the HS mode is much better than that in the NS and MS modes, which may be due to the high sensitivity to a weak echo of the Ka-band.

3) The comparisons of rainfall rate for liquid samples revealed that the performance of DPR NS and MS modes are similar, with correlations of approximately 0.58 and bias within 1 mm/h. The agreement of the MS mode is slightly better, especially for convective precipitation. This may be attributed to the best consistency in the D_m retrieval of the MS mode. The HS mode shows good consistency at stratiform precipitation despite relatively poor D_m retrieval performance. In contrast, the correlation coefficient for convective precipitation is only 0.39, with a bias that reaches -1.6 mm/h.

4) The rainfall relations of non-liquid hydrometeors of dry snow, wet snow, and graupel for CDP were obtained by scattering simulations. With the simulated rain relations, the mean biases

of rainfall estimate comparisons of non-liquid hydrometeors from CDP and DPR are within 1 mm/h. The NS mode exhibited the best agreement for the non-liquid rainfall estimation, followed by the HS mode. The agreement of rainfall estimation of non-liquid samples is worse than that of liquid samples on the whole, which may be because there are no special rainfall relations for non-liquid hydrometeors for DPR.

The comparison results show that the DPR NS, MS, and HS modes have advantages and disadvantages. The NS mode shows good comprehensive performance, with better agreement at comparing reflectivity, liquid, and non-liquid rainfall. The HS mode shows the best performance in stratiform precipitation because of its high sensitivity to low rainfall rates. At the same time, the MS mode performs best at convective precipitation, which may be attributed to its high accuracy of D_m retrieval with the DF method. Although the HS mode has a high sensitivity to light rain, it exhibits no obvious superiority in rainfall estimation of non-liquid hydrometeors. The comparison with respect to different hydrometeor phases shows that the rainfall estimation based on hydrometeor types is meaningful for both DPR and ground dual-polarization radar because the physical characteristics of different hydrometeors vary greatly. The rain relations between liquid and non-liquid precipitation are different. Furthermore, the comparisons in this study provide a basis for radar precipitation data error characterization and further optimal integration of multisensor data by capitalizing on the benefits from different sensors.

Acknowledgments

This study is jointly supported by the National Natural Science Foundation of China (41975027), the National Key Research and Development Program of China (2017YFC1501401), and a Project Funded by the Priority Academic Program Development of Jiangsu Higher Education Institutions (PAPD).

Data Availability Statement

The CDP data and the disdrometer data are from Nanjing University of Information Science and Technology and can be obtained by contacting the corresponding author (cassie320@163.com). The rain gauge data are from China National Meteorological Information Center and can be obtained by contacting the coauthor (chenaijun@nuist.edu.cn). The matched CDP data in this study and disdrometer data, rain gauge data are also available from

https://pan.baidu.com/s/1KeSaR7qFjz7C4erTjFxatQ with a code y646.The DPR data are available through https://www.nasa.gov/mission_pages/GPM/main/index.html.

References

Barros, A. P., Petersen, W., Schwaller, M., Cifelli, R., Mahoney, K., Peters-Liddard, C., et al. (2014). NASA GPM ground validation: integrated precipitation and hydrology experiment 2014 science plan. *NASA. Text*. https://dx.doi.org/10.7924/G8CC0XMR

Biswas, S. K., & Chandrasekar, V. (2018). Cross-validation of observations between the GPM dual-frequency precipitation radar and ground based dual-polarization radars. *Remote Sensing*, *10*, 1773. https://dx.doi.org/10.3990/rs10111773

Bolen, S. M., & Chandrasekar, V. (2003). Methodology for aligning and comparing spaceborne radar and ground-based radar observations. *Journal of Atmospheric and Oceanic Technology*, *20*(5), 647-659. https://dx.doi.org/10.1175/1520-0426(2003)20<647:MFAACS>2.0.CO;2

Brandes, E. A., Zhang G. F., & Vivekanandan J. (2002). Experiments in rainfall estimation with a polarimetric radar in a subtropical environment. *Journal of Applied Meteorology*, *41*(6), 674-685. https://doi.org/10.1175/1520-0450(2002)041<0674:EIREWA>2.0.CO;2

Bringi,V. N., & Chandrasekar, V. (2001). *Polarimetric Doppler weather radar: principles and applications*. New York, NY: Cambridge Univ. Press.

Camille, L. C., & Nick, G. (2020). Comparison of rainfall products over Sub-Saharan Africa. *Journal of Hydrometeorology*, *21*,553-596. https://doi.org/10.1175/JHM-D-18-0256.1

Cannon, F., Ralph, F. M., Wilson, A. M., & Lettenmaier, D. P. (2017). GPM satellite radar measurements of precipitation and freezing level in atmospheric rivers: comparison with ground-based radars and reanalyses. *Journal of Geophysical Research: Atmosphere*, *122*(12), 747-764. https://doi.org/10.1002/2017JD27355

Cao, Q., Zhang, G. F., Brandes, E. A., & Schuur T. J. (2010). Polarimetric radar rain estimation through retrieval of drop size distribution using a Bayesian approach. *Journal of Applied Meteorology & Climat*ology, *49*(5), 973-990. https://doi.org/10.1175/2009JAMC2227.1

Cao, Q., Hong, Y., Qi, Y. C., Wen, Y. X., Zhang, J., Gourley, J. J., & Liao, L. (2013). Empirical conversion of the vertical profile of reflectivity from Ku-band to S-band frequency. *Journal of Geophysical Research: Atmospheres*, *118*, 1814-1825. https://doi.org/10.1002/jgrd.50138

598 Cao, Y., Chen, H. B., & Su, D. B. (2018). Identification and correction of the bright band using a
599 C-band dual polarization weather radar. *Journal of Applied Meteorological Science*, *29*(1), 84-
600 96. https://doi.org/10.11898/1001-7313.20180108
601 Chandrasekar, V., Hou, A., Smith, E., Bringi, V. N., Rutledge, S. A., Gorgucci, E., Petersen, W.
602 A., & Jackson, G. S. (2008). Potential role of dual-polarization radar in the validation of
603 satellite precipitation measurements: rational and opportunities. *Bulletin of the American*
604 *Meteorological Society*, *89*(8), 1127-1146. https://doi.org/10.1175/2008BAMS2177.1
605 Chase, R. J., Nesbitt, S. W., & Mcfraquhar, G. M. (2020). Evaluation of the microphysical
606 assumptions within GPM-DPR using ground-based observations of rain and snow. *Atmosphere*,
607 *11*(6), 619-639. https://dx.doi.org/10.3390/atmos11060619
608 Chen, H. N., Chandrasekar, V., & Bechini, R. (2017). An improved dual-polarization radar rainfall
609 algorithm (DROPS2.0): application in NASA IFloods field campaign. *Journal of*
610 *Hydrometeorology, 18,* 917-937. https://dx.doi.org/10.1175/JHM-D-16-0124.1
611 Chen, Y., Kou, L. L., Jiang, Y. F., Yang, C. S., Lin, Z. J., & Chu, Z. G. (2021). Variational raindrop
612 size distribution retrieval from dual-polarimetric radar based on a new observation operator.
613 *Journal of Tropical Meteorology,* Accepted.
614 Cifelli, R., Chandrasekar, V., Lim, S., Kennedy, P. C., Wang, Y., & Rutledge, S. A. (2011). A new
615 dual-polarization radar rainfall algorithm: application in Colorado precipitation events. *Journal*
616 *of Atmospheric and Oceanic Technology*, *28*, 352-264.
617 https://dx.doi.org/10.1175/2010JTECHA1488.1
618 D'Adderio, L. P., Vulpiani, G., Porcu, R., Tokay, A., & Meneghini, R. (2018). Comparison of
619 GPM core observatory and ground-based radar retrieval of mass-weighted mean raindrop
620 diameter at Midlatitude. *Journal of Hydrometeorology*, *19*, 1583-1598.
621 https://dx.doi.org/10.1175/JHM-D-18-0002.1
622 D'Adderio, L. P., Porcù, F., Panegrossi, G., Marra, A. C., Sanò, P., & Dietrich, S. (2019).
623 Comparison of the GPM DPR single- and double-frequency products over the Mediterranean
624 area. *IEEE Transactions on Geoscience and Remote Sensing*, *57*(12), 9724-9739.
625 https://dx.doi.org/10.1109/TGRS.2019.2928871
626 Gao, Y., Wu, T. W., Wang, J., & Tang, S. H. (2021). Evaluation of GPM dual-frequency
627 precipitation radar (DPR) rainfall products using the rain gauge network over China. *Journal*
628 *of Hydrometeorology, 22*, 547-559. https://dx.doi.org/10.1175/JHM-D-20-0156.1

Giangrande, S., & Ryzhkov, A. V. (2008). Estimation of rainfall based on the results of polarimetric echo classification. *Journal of Applied Meteorology and Climatology*, *47*, 2445-2462. https://dx.doi.org/10.1175/2008JAMC1753.1

Hou, A. Y., Ramesh, K. K., Steven, N., Azararzin, A., Kummerow C. D., Kojima, M., Oki, R., Nakamura, K., & Iguchi, T. (2014). The global precipitation measurement mission. *Bulletin of American Meteorological Society*, *95*(5), 701-722. https://doi.org/10.1175/BAMS-D-13-00164.1

Houze, R. A., Mamurdie, L. A., Petersen, W. A., Schwaller, M. R., Baccus, W., Lundquist, J. D., et al. (2017). The Olympic mountains experiment (OLYMPEX). *Bulletin of the American Meteorological Society*, *10*, 2167-2188. https://doi.org/10.1175/BAMS-D-16-0182.1

Huang, H., Zhao, K., Zhang G. F., Hu D. M., & Yang, Z W. (2020). Optimized raindrop size distribution retrieval and quantitative rainfall estimation from polarimetric radar. *Journal of Hydrology*, *580*, 124248. https://doi.org/10.1016/j.jhydrol.2019.124248

Iguchi, T., Seto, S., Meneghini, R., Yoshida, N., Awaka, J., Le, M., Chandrasekar, V., Brodzik, S., & Kubota, T. (2017). *GPM/DPR Level-2 Algoirthm Theoretical Basis Document*. Available online: https://pps.gsfc.nasa.gov/Documents

Jiang, Y. F., Kou, L. L., Chen, A. J., Wang, Z. H., Chu, Z. G., & Hu, H. F. (2020). Comparison of reflectivity factor of dual polarization radar and dual-frequency precipitation radar. *Journal of Applied Meteorological Science*, *31*(5), 608-619. https://dx.doi.org/10.11898/1001-7313.20200508

Kou, L. L., Li, Y. C., Chu, Z. G., & Xu, F. (2018). C-band dual-polarization Doppler weather radar data analysis and its application in quantitative precipitation estimation. *Journal of Tropical Meteorology*, *34*(4), 460-471. https://dx.doi.org/10.16032/j.issn.1004-4965.2018.04.003

Kou, L. L., Wang, Z. H., & Xu, F. (2018). Three-dimensional fusion of spaceboren and ground radar reflectivity data using a neural network-based approach. *Advances in Atmospheric Sciences*, *35*(3), 346-359. https://doi.org/10.1007/s00376-017-6334-9

Lasser, M., Sungmin, O., & Foelshe, U. (2019). Evaluation of GPM-DPR precipitation estimates with WegenerNet gauge data. *Atmospheric Measurement Techniques*, *12*, 5055-5070. https://doi.org/10.5194/amt-12-5055-2019

Le, M., & Chandrasekar, V. (2013). Hydrometeor profile characterization method for dual-frequency precipitation radar onboard the GPM. *IEEE Transactions on Geoscience and Remote Sensing*, *51*(6), 3648-3658. https://doi.org/10.1109/TGRS.2012.2224352

Le, M., Chandrasekar, V., & Biswas, S. (2016). Evaluation and validation of GPM dual-frequency classification module after launch. *Journal of Atmospheric and Oceanic Technology*, *33*, 2699-2716. https://doi.org/10.1175/JTECH-D-15-0253.1

Liao, L., & Meneghini R. (2009). Changes in the TRMM Version-5 and Version-6 precipitation radar products due to orbit boost. *Journal of the Meteorological Society of Japan*, *87A*, 93-107. https://doi.org/10.2151/jmsj.87A.93

Liao, L., Meneghini, R., & Tokay, A. (2014). Uncertainties of GPM DPR rain estimates caused by DSD parameterizations. *Journal of Applied Meteorology and Climatology*, *53*, 2524-2537. https://dx.doi.org/10.1175/JAMC-D-14-0003.1

Liao, L., & Meneghini, R. (2019). Physical evaluation of GPM DPR single- and dual-wavelength algorithms. *Journal of Atmospheric and Oceanic Technology*, *36*, 883-902. https://doi.org/10.1175/JTECH-D-18-0210.1

Liu, L. P., Mu, R., Xu, X. Y., & Hu, Z. Q. (2007). Dynamic and microphysical structures of a squall line system and effects of rain drop size distribution on precipitation. *Acta Meteorologica Sinica*, *65*(4): 601-611. https://doi.org/10.3321/j.issn:0577-6619.2007.04.012

Mahale, V. N., Zhang, G. F., Xue, M., Gao, J., & Reeves, H. D. (2019). Variational retrieval of rain microphysics and related parameters from polarimetric radar data with a parameterized operator. *Journal of Atmospheric and Oceanic Technology*, *36*(12), 2483-2500. https://doi.org/10.1175/JTECH-D-18-0212.1

Park, S. G., Maki, M., Iwanami, K., Bringi, V. N., & Chandrasekar, V. (2005). Correction of radar reflectivity and differential reflectivity for rain attenuation at X band. Part II: evaluation and application. *Journal of Atmospheric and Oceanic Technology*, *22*, 1633-1655, https://doi.org/10.1175/JTECH1804.1

Park, H., Ryzhkov, A. V., Zrnic, D. S., & Kim, K. E. (2009). The hydrometeor classification algorithm for the polarimetric WSR-88D: description and application to an MCS. *Weather and Forecasting*, *24*, 730-748. https://doi.org/10.1175/2008WAF2222205.1

687 Petracca, M., D'Adderio, L. P., Porcu, F., Vulpiani, G., Sebastianelli, S., & Puca, S. (2018).
688 Validation of GPM dual-frequency precipitation radar (DPR) rainfall products over Italy.
689 *Journal of Hydrometeorology*, *19*, 907-925. https://dx.doi.org/10.1175/JHM-D-17-0144.1
690 Radhakrishna, B., Satheesh, S. K., Narayana Rao, T., Saikranthi, K., & Sunilkumar, K. (2016).
691 Assessment of DSDs of GPM-DPR with ground-based disdrometer at seasonal scale over
692 Gadanki, India. *Journal of Geophysical Research: Atmosphere*, *121*(11), 792-802.
693 https://doi.org/10.1002/2015JD024682
694 Schuur, T., Ryzhkov, A., Heinselman, P., Zrnic, D., Burgess, D., & Scharfenberg, K. (2003).
695 *Observations and classification of echoes with the polarimetric WSR-88D radar*.
696 NOAA/National Severe Storms Laboratory Report, Retrieved from
697 https://www.researchgate.net/publication/241142902
698 Seto, S., Iguchi, T., & Oki, T. (2013). The basic performance of a precipitation retrieval algorithm
699 for the global precipitation measurement mission's single/dual-frequency radar measurements.
700 *IEEE Transactions on Geoscience and Remote Sensing*, *51*(12), 5239-5251.
701 https://doi.org/10.1109/TGRS.2012.2231686
702 Skofronick-Jackson, G., Petersen W. A., Berg W., Kidd, C., Stocker, E. F., Kirschbaum, D. B., et
703 al. (2017). The global precipitation measurement (GPM) mission for science and society.
704 *Bulletin of the American Meteorological Society*, *98*(8), 1679-1696.
705 https://doi.org/10.1175/BAMS-D-15-00306.1
706 Skofronick-Jackson, G., Kirschbaum, D., Petersen, W., Huffman, G., Kidd, C., Stocker, E., &
707 Kakar, R. (2018). The global precipitation measurement (GPM) mission's scientific
708 achievements and societal contributions: reviewing four years of advanced rain and snow
709 observations. *Quarterly Journal of the Royal Meteorological Society*, *144*(1), 27-48.
710 https://doi.org/10.1002/qj.3313
711 Speirs, P., Gabella, M., & Berne, A. (2017). A comparison between the GPM dual-frequency
712 precipitation radar and ground-based radar precipitation rate estimates in the Swiss Alps and
713 Plateau. *Journal of Hydrometeorology*, *18*, 1247-1269. https://dx.doi.org/10.1175/JHM-D-16-
714 0085.1
715 Tang, G. Q., Wen, Y. X., Gao, J. Y., Long, D., Ma, Y. Z., Wan, W., & Hong, Y. (2017). Similarities
716 and differences between three coexisting spaceborne radars in global rainfall and snowfall

717 estimation. *Water Resources Research*, *53*, 3835-3853.
718 https://doi.org/10.1002/2016WR019961
719 Watters, D., Battaglia, A., Mroz, K., & Tridon, F. (2018). Validation of the GPM version-5 surface
720 rainfall products over Great Britain and Ireland. *Journal of Hydrometeorology*, *19*, 1617-1636.
721 https://doi.org/10.1175/JHM-D-18-0051.1
722 Wen, Y. X., Hong, Y., Zhang, G. F., Schuur, T. J., Gourley, J. J., Flamig, Z., Morris, K. R., & Cao,
723 Q. (2011). Cross validation of spaceborne radar and ground polarimetric radar aided by
724 polarimetric echo classification of hydrometeor types. *Journal of Applied Meteorology and*
725 *Climatology*, *50*, 1389-1402. https://dx.doi.org/10.1175/2011JAMC2662.1
726 Zhang, A. S., Xiao, L. S., Min, C., Chen, S., Kulie, M., Huang, C. Y., & Liang, Z. Q. (2019).
727 Evaluation of latest GPM-Era high-resolution satellite precipitation products during the May
728 2017 Guangdong extreme rainfall event. *Atmospheric Research*, *216*, 76-85.
729 https://doi.org/10.1016/j.atmosres.2018.09.018
730 Zhang, G. F., Vivekanandan, J., & Brandes, E. A. (2001). A method for estimating rain rate and
731 drop size distribution from polarimetric radar measurement. *IEEE Transactions on Geoscience*
732 *and Remote Sensing*, *39*(4), 830-841. https://doi.org/10.1109/36.917906